Large-Area Periodic Arrays of Atomically Flat Single-Crystal Gold Nanotriangles formed Directly on Substrate Surfaces

Robert D. Neal,[†] Zachary R. Lawson,[†] Walker J. Tuff,[†] Kaikui Xu,[†] Vishal Kumar,[‡] Matiyas T. Korsa,[§] Maksym Zhukovskyi,[∥] Matthew R. Rosenberger,[†] Jost Adam,[§] Jordan A. Hachtel,[&] Jon P. Camden,[‡] Robert A. Hughes,[†] and Svetlana Neretina[†‡]*

[†] College of Engineering, University of Notre Dame, Notre Dame, Indiana 46556, United States

[‡] Department of Chemistry and Biochemistry, University of Notre Dame, Notre Dame, Indiana 46556, United States

[§] Computational Materials Group, SDU Centre for Photonics Engineering, Mads Clausen Institute, University of Southern Denmark, 5230 Odense, Denmark

[∥] Notre Dame Integrated Imaging Facility, University of Notre Dame, Notre Dame, Indiana 46556, USA

[&]Center for Nanophase Materials Sciences, Oak Ridge National Laboratory, Oak Ridge, TN 37830, USA

*E-mail: sneretina@nd.edu

Keywords: nanotriangle, nanoplate, periodic array, gold, epitaxy, Brij-700

ABSTRACT. The advancement of nanoenabled wafer-based devices requires the establishment of core competencies related to the deterministic positioning of nanometric building blocks over large areas. Within this realm, plasmonic single-crystal gold nanotriangles represent one of the most attractive nanoscale components but where the formation of addressable arrays at scale has

heretofore proven impracticable. Herein, a benchtop process is presented for the formation of large-area periodic arrays of gold nanotriangles. The devised growth pathway sees the formation of an array of defect-laden seeds using lithographic and vapor-phase assembly processes followed by their placement in a growth solution promoting planar growth and three-fold symmetric side-faceting. The nanotriangles formed in this high-yield synthesis distinguish themselves in that they are epitaxially aligned with the underlying substrate, grown to thicknesses that are not readily obtainable in colloidal syntheses, and present atomically flat pristine surfaces exhibiting gold atoms with a close-packed structure. As such, they express crisp and unambiguous plasmonic modes and form photoactive surfaces with highly tunable and readily modeled plasmon resonances. The devised methods, hence, advance the integration of single-crystal gold nanotriangles into device platforms and provide an overall fabrication strategy that is adaptable to other nanomaterials.

1. Introduction

Single-crystal nanometals with a two-dimensional character form an architecturally diverse family of nanomaterials from which extraordinary structure-property relationships are derived.[1–6] Their existence is founded on the establishment of synthetic controls that are able to direct growth along highly anisotropic pathways that are counter to the symmetries of the underlying crystal structure. Referred to by such names as nanodisks,[7] nanoprisms,[5] nanoplates,[8,9] nanosheets,[10] and microflakes,[11,12] these structures can take on a variety of geometric forms including those that are irregular,[13] circular,[7] triangular,[5] hexagonal,[8] pentagonal,[14] spiral,[15,16] and star-like.[17] Among these, plasmonic nanotriangles (NTs) take on a prominent status due to (i) in-plane dipolar and higher order plasmon resonances that offer tunability throughout the visible and near-

infrared spectrum,[5,6,18] (ii) predictable behaviors based on variations to edge length,[6,19] thickness,[20,21] and aspect ratio,[6,20] (iii) intense electromagnetic near-field enhancements at their three corners,[22] (iv) a high refractive index sensitivity,[20] (v) tridirectional polarization-dependent scattering,[23,24] (vi) ultrafast nonlinear optical properties,[25] and (vii) remarkable coupling phenomena when placed in close proximity to similar[22] or dissimilar[26] structures. As such, the refinement of synthetic techniques that produce NTs that are able to fully and controllably express these plasmonic properties has taken on added importance.

The vast majority of Au NT growth modes directed toward the synthesis of plasmonic structures utilize solution-based methods. Essential to the success of these colloidal techniques is the implementation of synthetic controls that (i) promote planar growth, (ii) establish and maintain the required faceting, and (iii) purify the reaction product. The realization of planar growth is reliant on the formation of either preformed or spontaneously nucleated seeds with stacking faults defects that disrupt the ABCABC… stacking sequence that occurs along the [111] axis of a face centered cubic (fcc) metal. It is the protrusion of these planar defects at the periphery of the seed as low-energy reentrant grooves that provide the break in symmetry needed to promote lateral growth.[5,27] With the required seeds in place, suitably chosen capping agents direct the synthesis toward a triangular product with two large-area (111) facets. Cetyltrimethylammonium bromide (CTAB), cetyltrimethylammonium chloride (CTAC), and halide ions are typically used for this purpose[5] but where notable exceptions occur.[28,29] Even though such shape-directing agents have proven highly effective, the reaction product is compromised by structures having a three-dimensional character because it has proven difficult to produce uniformly-sized defect-laden seeds in high yield. This has necessitated the need for shape-purification procedures, with depletion flocculation[30,31] and centrifugation in the presence of a NaCl additive[32] both giving

rise to exceptionally high yields. Current methods for the preparation of seeds are also deficient in that they allow for limited variability in their diameter. This is significant because it is the seed diameter that is largely responsible for determining the NT thickness, a parameter of significance when tuning the localized surface plasmon resonance (LSPR) in the visible spectrum.[20] As a result, thin NTs with a range of thicknesses have been produced[28] while the synthesis of thicker plates (> 20 nm) require specialized two-stage procedures where they are first synthesized and then isotropically enlarged using a secondary colloidal chemistry.[20,21] A more appealing approach would allow for the NT edge-length and thickness to be adjusted as independent variables.

The integration of single-crystal nanometals with wafer-based processing techniques has taken on a newfound importance due to breakthrough capabilities and the advanced functionalities they have enabled.[1,33–36] Among the various nanocrystal geometries, noble metal nanoplates provide an especially appealing architecture since its planar character matches that of the substrate, an attribute that has already been a decisive factor in advancing numerous applications.[1] The majority of these efforts have relied on colloid-to-substrate transfers to populate substrate surfaces with single-crystal nanoplates. Although their placement on substrates in random configurations is straightforward, forming organized configurations has proven difficult. Advances are, however, occurring for self-assembly techniques yielding substrate-based Au NTs in close-packed configurations.[28,32,37–39] In contrast, only two reports by Mirkin and co-workers[40,41] have been responsive to the challenge of forming periodic arrays of Au NTs in which they use lithographically-defined trapping sites to capture and orient structures from a colloidal suspension. These demonstrations, while undeniably impressive, have only yielded sub-square-millimeter arrays, require the use of the technically demanding e-beam lithography method, and can only be

practiced on substrate materials amenable to these techniques (e.g., Si, PDMS, Au−Cr layers). There is, hence, opportunities to advance solutions that address these drawbacks.

An alternate approach to the placement of colloidal nanoplates on substrate surfaces is to form seeds with the required stacking fault defects directly on a substrate followed by their exposure to liquid-state syntheses promoting planar growth. In some of the earliest studies, Zamborini and co-workers[42] demonstrated this conceptually appealing approach but it has received little traction due to an inability to generate the required seeds in high yield. More recently, Golze et al.[43] overcame this hurdle by using heteroepitaxial interactions occurring at the Au-substrate interface as the primary driver for generating identically oriented Au seeds with the required internal defect structure. Herein, we capitalize on this breakthrough in demonstrating a first-of-its-kind synthesis in which single-crystal Au NTs are prepared directly on substrate surfaces in large-area periodic arrays. The so-formed structures exhibit epitaxy-induced alignment, atomically flat surfaces, and allow for LSPR tuning based on the independent control of NT thickness and edge-length. The work, therefore, forwards the nanofabrication techniques needed to exploit one of the foremost building blocks in the study and application of plasmonic materials.

2. Results

Figure 1a,b shows a schematic of the five-step benchtop process used to fabricate periodic arrays of single-crystal Au NTs along with optical images of the substrate taken after each step. In this procedure, nanoimprint lithography, in combination with reactive ion etching (RIE), is first used to form a hexagonal array of cylindrical holes[44] that extend through a bilayer resist to the surface of a [0001]-oriented sapphire (i.e., Al_2O_3) substrate. Sb and Au layers are then sequentially sputter deposited over the entire patterned surface, followed by a lift-off procedure that removes

the remaining resist to reveal cylindrical disks of Sb topped with a thin layer of Au. The disks are then exposed to a high-temperature vapor-phase assembly process that causes each of them to assemble into a single-crystal Au nanostructure as the Sb is lost to the vapor phase. Sb, while sacrificial, is crucial to array definition since multiple Au nanostructures appear near each of the array positions when the same procedure is carried out in its absence.[45] The Au nanostructure array then acts as seeds for a three-reagent liquid-phase synthesis of aqueous $HAuCl_4$, Brij-700, and CTAB that promotes planar growth with three-fold symmetric side-faceting. Optimal NT arrays occurred for a 35 °C growth solution with $HAuCl_4$, Brij-700, and CTAB concentrations of 0.86, 4.38, and 1.08 mM, respectively. Figure 1c−e shows SEM images of the so-formed array. It reveals that NTs with sharp corners are formed in high yield with a high degree of in-plane alignment where each points either in an upward or downward direction (Figure 1d). Some of the arrayed structures, however, have truncated corners or three-dimensional morphologies. With long-range order occurring over an area that spans 8 mm × 8.35 mm, the periodic array establishes a new benchmark in terms of large-area capabilities for NTs that eclipses prior demonstrations[41] by nearly 200-fold.

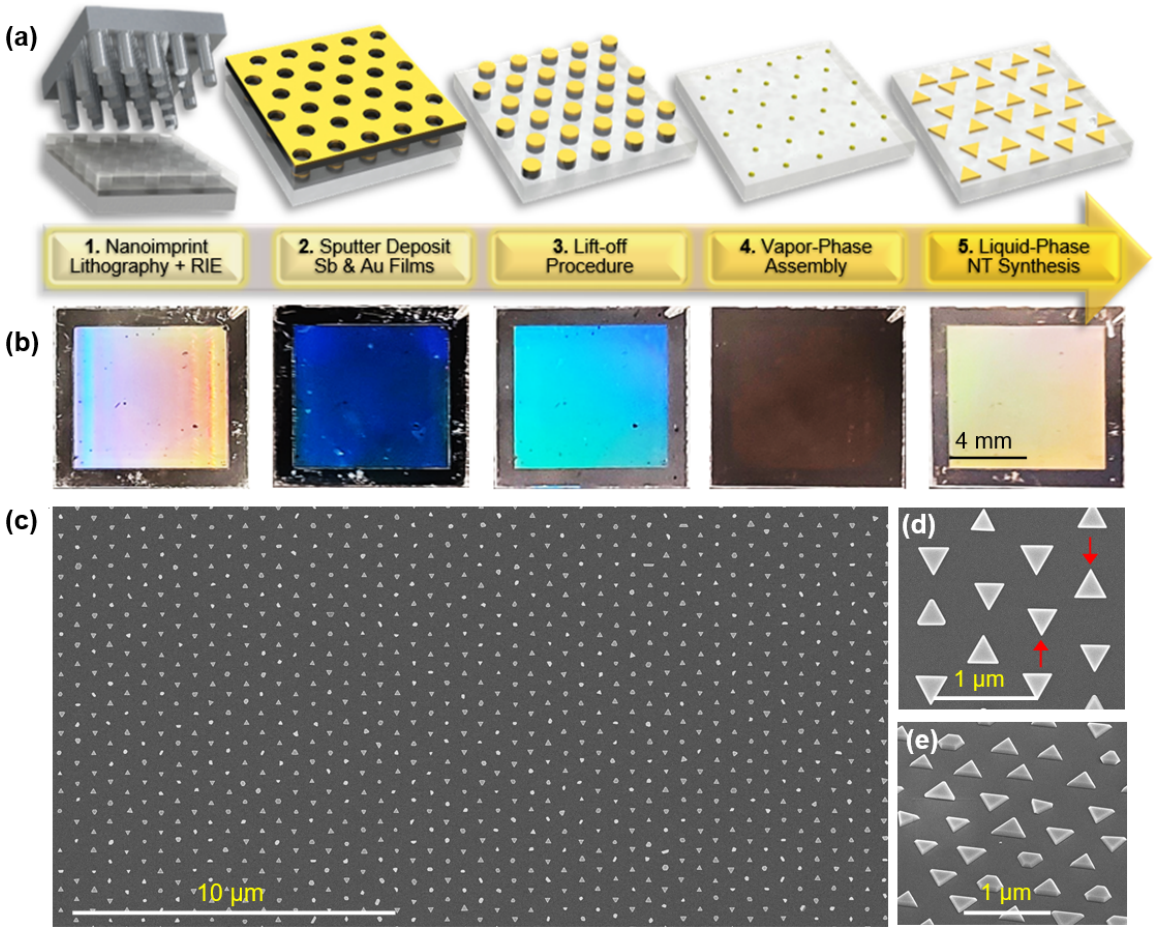

Figure 1. (a) Schematic of the five-step procedure used to fabricate periodic arrays of Au NTs. (b) Optical images of the substrate taken after the completion of each step in the procedure where the final image in the progression is the NT array. (c) Low-magnification SEM image of a NT array. High-magnification images showing (d) top and (e) tilted view SEM images of NTs.

From a mechanistic standpoint, the emergence of NTs is contingent on the synthetic controls imposed by interfacial interactions between (i) Au and the underlying substrate occurring during seed formation and (ii) the components of the growth solution and the Au seeds occurring during the liquid-phase NT synthesis. During seed formation, it is the heteroepitaxial relationship formed between the (111) planes of Au and the (0001) surface of sapphire[46] that is largely responsible for the emergence of NTs that lie flat on the substrate surface in one of two equally probable in-plane orientations offset by 180° (denoted by the red arrows in Figure 1d).[47] Additionally, it is the Au−substrate interactions occurring during seed assembly that result in seeds that are lined

with stacking fault defects that preferentially form along the [111] Au axis that is normal to the substrate surface.[43] With these defects in place, there is the required break in symmetry needed to induce a two-dimensional growth mode with a growth trajectory that is parallel to the substrate surface. The unwanted three-dimensional structures appearing in the array are caused by defective seeds that do not meet these criteria.[43] Once the seeds are immersed into the growth solution, they are reliant on the interplay between the three reagents if they are to emerge as NTs where $HAuCl_4$ acts as the metal precursor, Brij-700 as the reducing agent, and Brij-700 and CTAB as shape-directing agents. The need for two shape-directing agents makes this aspect somewhat convoluted but some clarity stems from the fact that the synthesis, when performed in the absence of CTAB, yields mostly hexagonal nanoplates (Figure S1). CTAB is therefore required to promote the three-fold symmetric side-faceting but is not needed in maintaining the planar geometry. It should also be noted that this substrate-based NT growth mode differs from its colloidal counterparts in that the reagent concentrations remain near-constant over the course of the reaction because they are supplied in quantities that far exceed those used in the synthesis. The reaction is, hence, terminated not by the consumption of reactants but by the mere removal of the substrate from the growth solution. Apart from an initial yellow-to-orange color change occurring in the first 30 min, the growth solution remains constant in color for syntheses lasting as long as 7 h.

The crystallinity of the NTs was assessed using TEM characterization. For these measurements, NTs were prepared directly on silicon nitride (Si_xN_y) TEM grids using Au seeds formed in random configurations. Although the yield is considerably lower when forming structures on the amorphous Si_xN_y surface, NTs are nevertheless produced in sufficient quantities for single-particle characterization. Figure 2a shows a low-magnification TEM image of four NTs having edge lengths between 320 and 400 nm. A bright-field TEM image of an individual NT

(Figure 2b) reveals somewhat rounded corners and shows no evidence of dislocation defects. Selected-area electron diffraction (SAED) performed on the same structure shows the {220} reflections expected for a NT with its [111]-direction perpendicular to the underlying surface (Figure 2c). Also observed are six weak ⅓{422} reflections that are nominally forbidden for a face-centered cubic (fcc) crystal but which appear when stacking fault defects are present along the [111] zone axis. The result, hence, confirms that the symmetry-breaking defects responsible for the two-dimensional growth mode[5,27] are present in these structures. Figure 2d shows a high-resolution TEM (HRTEM) image taken where the (111) top and (100) side facets meet (denoted by the green box in Figure 2b). It reveals both crisp faceting and the anticipated {220} lattice fringes with a 1.4 Å spacing. Overall, the TEM data shows that, apart from the required stacking fault defects, the NTs have a highly faceted single-crystal character.

The preparation of Au NTs directly on a Si_xN_y TEM grid also allowed for an nanoscale assessment of their plasmonic properties by performing electron-energy loss spectroscopy inside a scanning transmission electron microscope (STEM-EELS). Figure 2e shows a high-angle annular dark-field (HAADF) image of a single Au NT on which beam positions corresponding to the NT vertex, center-point, and edge center-point are denoted. EEL profiles corresponding to these locations are shown in Figure 2f. The profile obtained for the beam positioned at the NT vertex (blue trace) exhibits four sharp plasmon modes, i.e., n = 1 (0.67 eV), n = 2 (1.25 eV), n = 3 (1.67 eV), and n = 4 (1.89 eV). The corresponding EEL spectrum images, showing the spatial distribution for the n = 1, 2, and 3 modes, are displayed in Figure 2g. In agreement with previous studies[48–50] is the observation of a dipolar mode (n = 1) with a strong energy-loss intensity near the NT corners and a quadrupole mode (n = 2) that additionally displays high intensity at the edge center-points. The n = 3 mode, which displays three nodes at each side of the nanostructure,

corresponds to a higher order multipolar mode whose observation signifies that the NT is of high quality. When the electron beam is placed near the NT edge center-point (green trace), the EEL profile shows intense peaks for even-numbered modes (n = 2, 4) because these modes have a high loss intensity at these center-edge positions, as is evident from the spectrum image for the quadrupole mode (i.e., n = 2, 1.25 eV). The relatively weak dipole peak is due to the diffuse scattering occurring when modes are confined to the corners of the NT.[51] When the electron beam is positioned at the center of the NT (red trace), it exhibits two strong peaks corresponding to the bulk plasmon (2.34 eV)[52] and the quadrupole mode (1.25 eV). Taken together, these EEL measurements show behaviors that are consistent with those observed for colloidal NTs and confirm that high plasmonic activity is exhibited by these substrate-grown structures.

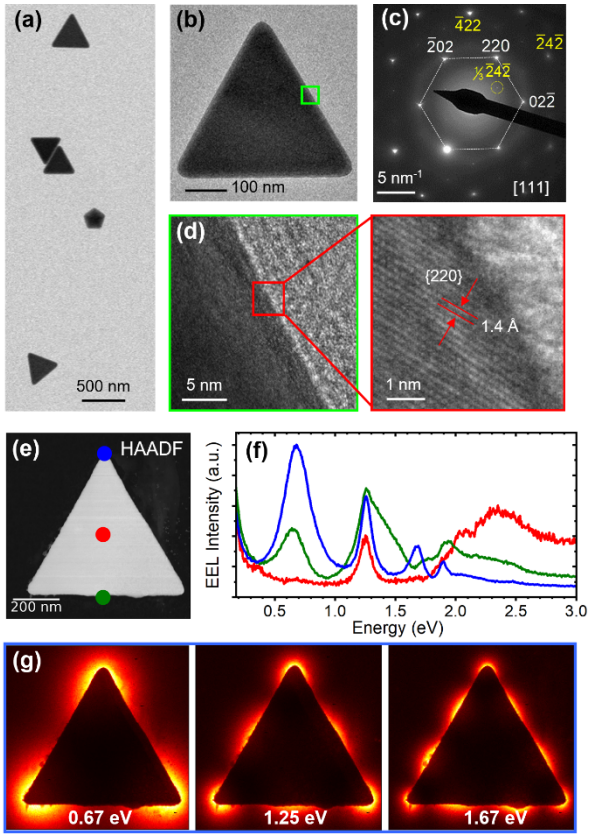

Figure 2. (a) Low-magnification TEM image of Au NTs formed directly on a Si_xN_y TEM grid. (b) Bright-field TEM image of a single NT and (c) its corresponding SAED pattern. (d) HRTEM images of the region where the (111) top and (100) side facet meet. (e) HAADF image of a single Au NT marked with the three electron beam positions investigated. (f) Energy-loss profiles corresponding to each of the three beam positions. Values corresponding to the center position (red) have been divided by two for the purpose of clarity. (g) EEL spectrum images showing the spatial distribution of the n = 1 (0.67 eV), n = 2 (1.25 eV), and n = 3 (1.67 eV) plasmon modes.

Atomic force microscopy (AFM) measurements were used to assess the height profiles of the arrayed structures. The topographical map, shown in Figure 3a, reveals NTs expressing a high degree of height uniformity as well as unwanted three-dimensional structures that protrude further from the surface. The line scan taken across four NTs (Figure 3b) shows near-identical NT thicknesses of approximately 50 nm. This level of consistency in height, which is preserved for growth times as long as 7 h (Figure 3c), demonstrates both the effectiveness of the lithographic process in establishing identically sized seeds and the ability of the capping agents in inhibiting

nanoplate growth in the vertical direction. Also noteworthy is that the NT thickness is considerably larger than is typically obtained in colloidal syntheses. Figure 3d shows a height profile extending from the surface of the substrate, along the edge of the NT, and ending at the top surface of the NT. With an edge slope of 54.8°, the result is consistent with the 54.7° angle expected for a [111]-oriented NT with [100]-oriented side facets, as is shown schematically in the inset to Figure 3d. The top planar surfaces of the NTs are atomically flat, showing root-mean-square roughness values ranging from 0.05 to 0.08 nm (Figure S2). Figure 3e shows a fast Fourier transform (FFT) autocorrelated atomic stick-slip AFM image of the (111) surface of the NT. The image reveals the pattern expected for the hexagonal close-packed (111) plane of Au. An analysis of the pattern in which the six nearest neighbor distances was determined for all atoms except those on the edge (≈ 1050) revealed an average interatomic distance of 0.2885 nm. This value is almost in exact agreement with the 0.2884 nm nearest neighbor distance expected for bulk Au.[46] The image also compares well with that obtained for single crystals of Au formed using a high-temperature surfactant-free vapor-phase synthesis.[53]

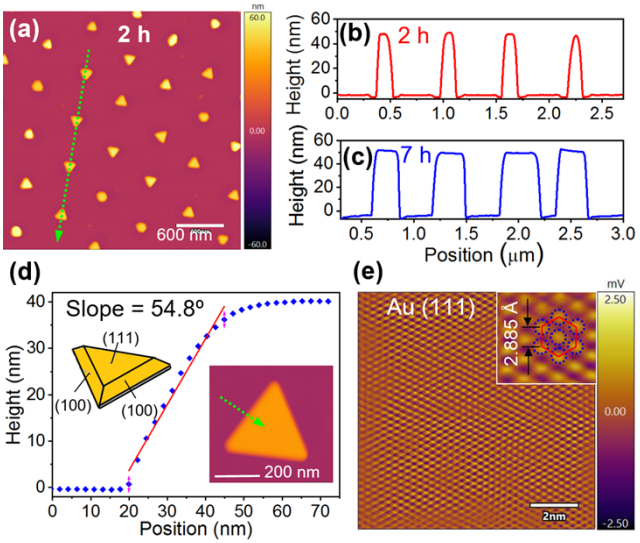

Figure 3. (a) Topographic AFM image of a Au NT array. AFM line scans showing the height profiles for four adjacent NTs grown for (b) 2 and (c) 7 h. (d) Line scan across a single edge of a NT (green arrow) that expresses the slope expected for the NT whose faceting is schematically illustrated in the inset. (e) FFT autocorrelated atomic stick-slip AFM image of the (111) surface of the NT that exhibits the atomic arrangement expected for a hexagonal close-packed (111) Au surface where the inset shows an expanded view.

With the NT dimensions being the primary determining factor in tuning the plasmon resonance to a specific value, syntheses were carried out in which the growth time was systematically varied. For these studies, periodic arrays of seeds were cut into smaller pieces and inserted into a single growth solution. Then, in a process that is analogous to the removal of aliquots in a colloidal synthesis, individual pieces were successively removed from the growth solution at 1 h intervals and examined using both AFM and SEM. Figure 4a provides a sequence of AFM images that show the emergence of a NT from a roundish seed followed by a steady increase in its edge length. Both the flat upper surface of the NT and its downward sloping side facets are clearly visible in the images. Figure 4b shows a height profile for each of the structures where it is evident that the initial seed height sets the NT thickness for the entire duration of the synthesis. Figure 4c shows the time progression of the NT edge length where each data point was derived from a statistical analysis of over 100 structures viewed in SEM images (representative images are shown in Figure

S3). A linear dependency is observed for edge lengths up to 400 nm. Determining whether this linear dependency continues beyond 400 nm was not possible because the 600 nm center-to-center spacing of the array leads to the collision of growth fronts between adjacent NTs. It is, however, anticipated that the edge length versus growth time curve would eventually round off as the reactants become depleted.

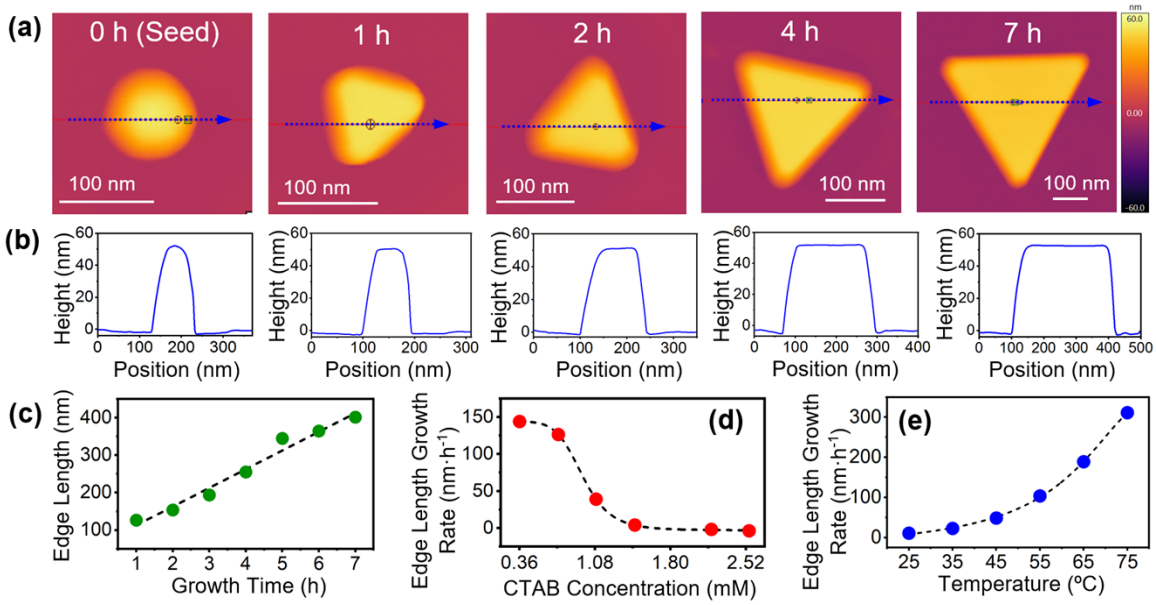

Figure 4. (a) Time series of AFM images showing the transformation of a Au seed into a NT followed by growth that increases its lateral dimensions. It should be noted that the scale bar varies between images. (b) Height profiles of each of the structures taken along the dashed blue arrows in Figure 3a. (c) Time dependence of the NT edge length under optimum synthesis conditions. NT edge length average growth rate as a function of the (d) CTAB concentration and (e) temperature.

With CTAB being essential to the NT growth mode, syntheses were carried out where its concentration was varied around the optimal value of 1.08 mM while leaving all other growth parameters unchanged. Figure 4d shows a plot of the NT edge length growth rate as a function of the CTAB concentration. Observed is a growth rate that steadily decreases as the CTAB concentration is increased. For concentrations that are lower than the optimal value, there is a substantial increase in the growth rate but this advantageous property is offset by a significant loss in NT yield to nanoplate structures expressing a hexagonal geometry (Figure S4). For

concentrations that are higher than the optimal value, the growth rate becomes diminished and even turns negative in that the seeds entering the growth solution are larger than those that exit (Figure S5). The loss of Au to oxidative etching is well-known[54] but where it is anticipated that such influences are exaggerated in the current work when compared to seed-mediated colloidal syntheses since there is only microgram quantities of Au existing as seeds on the substrate. Thus, while CTAB is effective as a NT shape-control agent, there exists just a narrow window of concentrations where the fine balance between yield and growth is achievable. It is noteworthy that many of these same trends have been observed when using CTAB in colloidal NT syntheses.[21]

The temperature at which the synthesis is carried out also has a pronounced effect upon NT growth. Figure 4e shows the temperature dependence of the NT edge length growth rate under optimum reactant concentrations for synthesis temperatures ranging between 25 and 75 °C. At 25 °C, the reaction product is nearly identical to the seed, indicating that essentially no growth occurs. Prominent NTs are formed over the rest of the temperature range where a more than ten-fold enhancement to the growth rate occurs between 35 and 75 °C. This increase is, however, accompanied by a gradual decline in the NT yield at the expense of nanoplates having irregular geometries (Figure S6). As such, a growth temperature of 35 °C was deemed optimal as it provided the highest yield while the relatively slow growth rate ensured that the growth time acted as a reliable control for adjusting NT dimensions.

By periodically removing and then reinserting a sample from the growth solution, it was possible to monitor the extinction spectrum as the NT edge length grew in size. Figure 5a shows the spectra obtained over a 6 h duration. The time series shows a plasmon resonance that both red-shifts and strengthens as its width first sharpens and then broadens. Extracted from the data is a

linear dependence in the plot of the LSPR peak position versus growth time (Figure 5a, inset) but where there exists an initial 1 h period where little to no growth occurs. Simulations of the extinction spectra for NTs as a function of edge length (Figure 5b) exhibit the same overall trends as the experimental data where a linear dependence is observed in a plot of the LSPR peak position versus edge length (Figure 5b, inset). The linearity revealed for both dependencies indicates that the NT edge length grows linearly in time, an outcome that is corroborated by the experimental data presented in Figure 4c. Moreover, the linearity exhibited by the LSPR peak position as a function of edge length is in agreement with that observed[55.56] and calculated[19,57] for colloidal and lithographically patterned NTs. A close inspection of the simulated spectra reveals the existence of higher order modes that are not readily apparent in the experimental data due to plasmon broadening effects arising from NT corner truncation,[58] size variations, and nontriangular shapes. In general, such modes are not readily observed for low aspect ratio nanoplates[59,60] due to significant mode overlap. As a final comment, it is noted that the NTs produced in this study provide a readily modeled dielectric environment since they lie flat on the substrate whereas colloidal structures, when placed either on flat substrates or in lithographically defined trenches, can exist in a dielectric environment that varies from NT to NT due to slight tilts or the degree to which the NT contacts the trench sidewalls. Smith et al.[61] have convincingly demonstrated that such influences can lead to a break in symmetry that promotes plasmon mode splitting.

The epitaxy-induced alignment of the NTs relative to the underlying substrate offers an ideal platform for assessing polarization-dependent responses. It should, however, be recognized that there exist two NT orientations offset by 180° (Figure 1d), and as such, their interactions with light will also be out of phase by 180°. Extinction measurements and simulations both show no obvious

polarization dependence (Figure S7). This result is in agreement with both theoretical and polarization-dependent spectroscopy measurements performed on lithographically-defined NTs that reveal two degenerate dipole modes offset by 90° where the response at intermediate angles is characterized by a superposition of these two fundamental modes.[61,62] Unexpected, is the observation that the refractive index sensitivity of the NTs shows a pronounced and highly reproducible polarization dependence (Figure 5c) in which values corresponding to the polarization along the NT vertex are about 7% higher than those for polarizations along its edge.

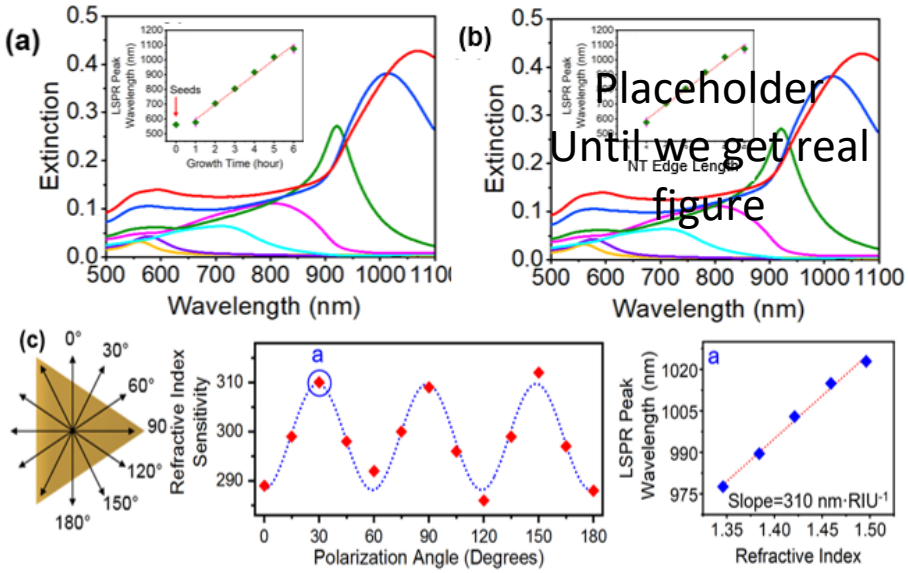

Figure 5. (a) Time-dependent extinction spectra for a NT growth lasting 6 h where the inset shows a linear dependency in the LSPR peak frequency with time. (b) Simulated extinction spectra for X nm thick NTs having various edge lengths where the inset shows a linear dependency in the LSPR peak frequency with edge length. (c) Polarization dependence of the refractive index sensitivity where the schematic illustrates NT alignment relative to the polarizer. The rightmost plot shows representative data for the 30° polarization from which a refractive index sensitivity of 310 nm·RIU^{-1} is extracted.

With the seed size largely determined by the amount of Au that is sputter deposited into the lithographically-defined openings, it becomes a relatively straightforward task to controllably vary its dimensions. In doing so, it presents the opportunity to treat the NT thickness and edge-length as independent variables since the former sets the thickness while the latter is determined by the

growth time. Noteworthy is that colloidal growth modes directed toward the synthesis of thick NTs have not yet been able to achieve independent control but where its potential benefit in terms of tailoring the plasmonic properties in the visible spectrum is well-recognized.[20,21,28] In demonstration of this capability, Au seed arrays with five different sizes were prepared. Spectroscopic characterization of the seeds show that, as expected, the LSPR red shifts and grows in strength as the seed diameter increases (Figure 6a). SEM images reveal average diameters of 60, 83, 86, 101, and 113 nm (Figure S8) while AFM characterization yields seed heights of 36, 48, 56, 66, and 78 nm (Figure 6b). The fact that the seed heights are smaller than the diameters is caused by the apparent truncation of the sphere morphology at the Au−substrate interface. The subsequent exposure of the various seed arrays to the growth solution results in NTs of variable thicknesses (Figure 6c). Spectroscopic data taken for the five samples over the course of the 5 h growth sees the LSPR red shift and strengthen over time (Figure S9) in a manner analogous to that shown in Figure 5a. Plots of the LSPR peak wavelength versus time (Figure 6d) for each NT thickness all show similar behavior in that there is little change in the first hour, followed by a linear dependency where the slope of the line increases as the thickness decreases. The average NT growth rate over the 5 h interval (Figure 6e) remains largely unchanged for NT thicknesses up to 60 nm but then shows a significant falloff. A plausible explanation for this behavior is that the lateral growth rate for thinner structures is limited by the capping agent since its coverage on the side-facets is essentially the same for all thicknesses, whereas the growth rate for similarly capped thicker structures is limited by a growth solution that cannot maintain an adequate supply of Au ions in the vicinity of the much larger NT growth front.

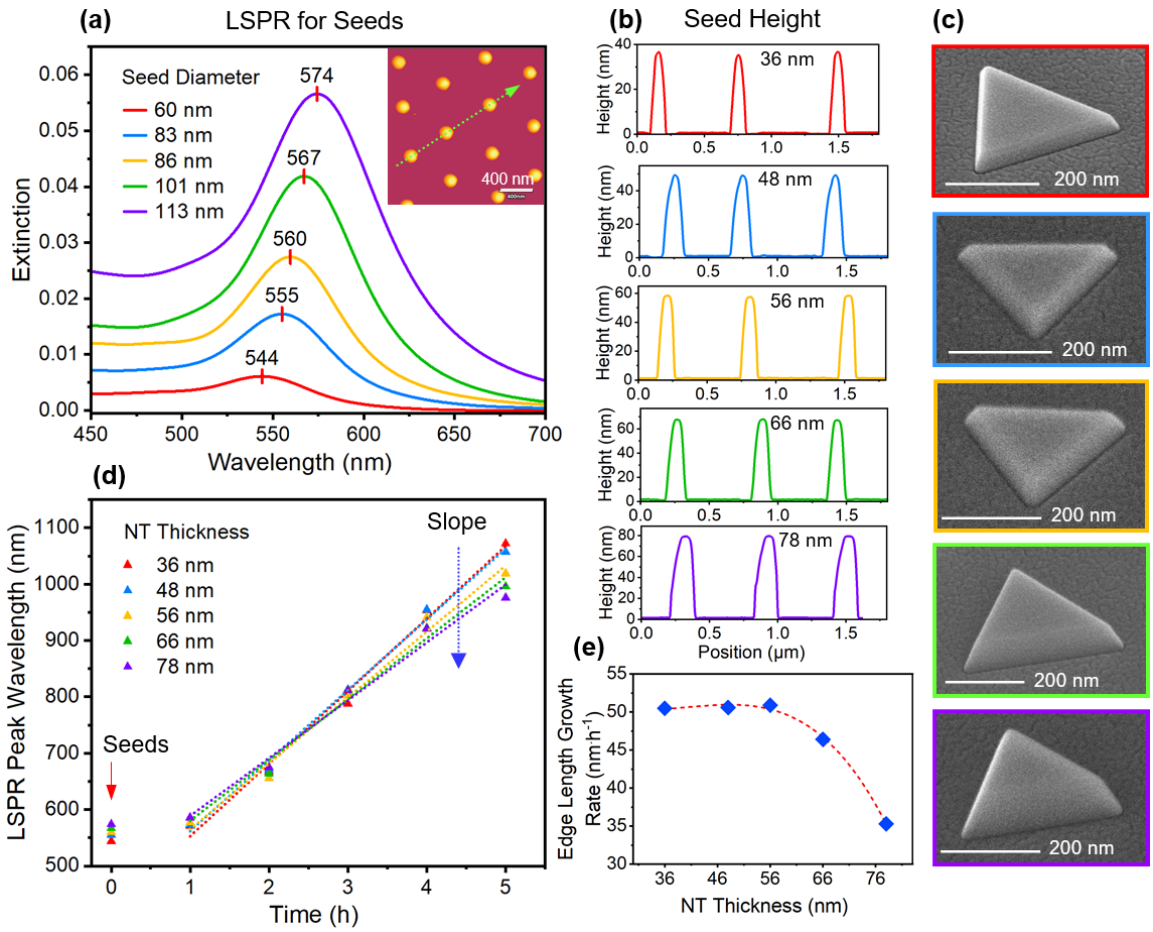

Figure 6. (a) Extinction spectra and (b) AFM height profiles for Au seeds of varying heights. The inset to Figure 6a shows a representative AFM trace. (c) SEM images showing NTs derived from each of the seeds. (d) Time dependence of the LSPR peak wavelength when each of the five seed sizes is subjected to the NT growth solution. (e) Average NT growth rate as a function of NT thickness.

3. Discussion

With the advent of this new approach for preparing Au NTs, a discussion of its strengths and weaknesses is warranted. When compared to the colloidal synthesis of Au NTs, the substrate-based approach offers advantage in that the seeds produced have diameters that are larger than those accessible to solution-based synthesis, and as such, provide the means to synthesize thicker NTs without resorting to two-stage procedures.[20,21] Additionally, the substrate-based synthesis lends itself to the independent control over NT thickness and edge-length. The colloidal approach is,

however, currently able to achieve thinner nanoplates than those accessible to the new approach. Even though the yield of seeds with the required stacking fault defects is quite high when compared to colloidal methods,[30–32] the requirement placed on yield is far more demanding since substrate-immobilized NTs are not amenable to standard post-synthesis purification schemes. The NT synthesis, therefore, is in need of further refinements in terms of yield along with improvements in size and shape uniformity if it is to be competitive with leading-edge colloidal NT growth modes that are subjected to purification procedures.[30,32] It is, however, of significance that the NT synthesis forwarded in this study realizes structures, which after a mere rinse in solvents, present (111) surfaces that are atomically flat, as is exemplified by the close-packed arrangement of Au atoms observable in AFM measurements. This is in contrast to other NT syntheses where surfaces are compromised by capping agents that can decisively influence physicochemical properties.[63]

Even more favorable comparisons are made when the current techniques are weighed against competing substrate-based platforms. Previously demonstrated methods for forming periodic arrays of single-crystal Au NTs require colloid-to-substrate transfer processes where NT colloids populate shallow triangular trenches formed on a substrate surface.[40,41] With trench fabrication requiring e-beam lithography, such methods become technically demanding, time-consuming, cost-prohibitive, and only realizable over small areas. Moreover, the arrays suffer from (i) vacancies, (ii) the in-plane misalignment of NTs originating from the need for oversized trenches in the assembly process, and (iii) a rather complicated and variable dielectric environment around each NT. In contrast, the current approach realizes large-area arrays using benchtop methods without the use of cleanroom facilities. The NTs show a high degree of in-plane alignment due to heteroepitaxy, lie flat on the substrate, and maintain a consistent and readily modeled dielectric environment. The existence of two equivalent heteroepitaxial relationships between Au and

sapphire do, however, lead to NTs with two in-plane orientations offset by 180°, an occurrence that is not inherent to the e-beam lithographic techniques. Substrate-based Au NT arrays have also been produced using lithographic technique in combination with the physical vapor deposition (PVD) of polycrystalline Au.[64,65] The majority of these demonstrations rely on e-beam lithography and, as a consequence, are similarly disadvantaged in terms of cost, scalability, and throughput. The use of low-cost colloidal lithographies[66,67] to define polycrystalline NT arrays offset these disadvantages but where true long-range order is sacrificed. More significant, however, are the well-documented advantages of single-crystal nanostructures when compared to those that are polycrystalline where the former offers (i) sharper corners capable of supporting larger local electromagnetic field enhancements, (ii) reduced plasmon damping due to smoother surfaces and the absence of adhesion layers, (iii) surfaces that support facet-dependent catalysis and functionalization, (iv) higher optical and thermal damage thresholds, and (v) superior device processing characteristics related to etching, ion milling, and the formation of crisp interfaces with subsequently deposited overlayers.[35,68−71]

4. Conclusion

In summary, a benchtop nanofabrication route has been devised for forming large-area periodic arrays of single-crystal Au NTs directly on substrate surfaces. The nanofabrication route forwarded is unique in that a three reagent liquid-phase synthesis has been discovered that, when practiced on substrate-immobilized seeds, gives rise to three-fold symmetric planar growth along the surface of the substrate. The approach provides an attractive alternative to the technically demanding processes that form periodic arrays of NTs by populating lithographically-defined trenches using colloid-to-substrate transfer mechanisms. By further employing the unique synthetic controls

accessible through lithographic and high-temperature directed-assembly techniques, NT syntheses becomes amenable to the independent control over thickness and edge-length, and in doing so, allows for greater optical tunability and NT dimensions that lie outside the range of those currently accessible to colloidal techniques. Other NT properties of significance include the straightforward removal of capping agents, atomically flat top surfaces, and a heteroepitaxy-induced alignment that gives rise to polarization-dependent optical properties. Taken together, the work advances the practices and knowhow needed to fully exploit one of the most important nanostructure architectures and, from a broader perspective, contributes to an ongoing effort that sees single-crystal nanomaterials integrated into device platforms.

5. Experimental Section

Materials. Au NTs were grown on two-side polished [0001]-oriented sapphire substrates with dimensions of 10 mm × 10.5 mm × 0.65 mm that were diced from 100 mm diameter wafers (MTI Corp.). The Sb target used for sputter depositions was cut from a 19 mm diameter rod with 99.999% purity (ESPI Metals). A similarly sized Au sputter target was punched from a 0.5 mm thick Au foil (99.9985% purity, Alfa Aesar). Au seed assembly was carried out in ultrahigh purity Ar (Airgas). The solution-based chemical synthesis of Au NTs used tetrachloroaurate (III) trihydrate ($HAuCl_4 \cdot 3H_2O$, 99.99% trace metal basis, Beantown Chemical), hexadecyltrimethylammonium bromide (CTAB, > 99% purity, Sigma-Aldrich), Brij-700 block copolymer (Average MW 4,670, Spectrum Chemicals), and deionized (DI) water with a resistivity of 18.2 MΩ·cm. The nanoimprint lithography process used a bilayer resist composed of mr-I 7030R (Micro Resist Technology) and polydimethylglutarimide (PMGI SF 3S) as well as a 40% CD−26 developer (Kayaku Advanced Materials). Nanoimprint lithography stamps were sourced

from Lightsmyth Technologies, after which a trichloro(1H, 2H, 2H-perfluorooctyl)silane (MilliporeSigma) antisticking layer was applied. TEM work was carried out using 20 nm thick silicon nitride grids (SIMPore Precision Membrane Technologies). Refractive index sensitivity measurements used toluene (Beantown Chemical) and acetonitrile (BDH Chemicals).

Au Seed Fabrication. Periodic arrays of Au seeds were fabricated using a modified version of our previously reported process.[43,44] The essence of the overall process has not changed in that nanoimprint lithography is used to define a hexagonal array of Au−Sb disks that, when heated, assemble into an array of crystalline Au nanostructures as the sacrificial Sb component is lost to the vapor phase. The modification made in the current study is that nanoimprint lithography is carried out using a bilayer resist[72] instead of a single-layer resist. The bilayer consists of two sequentially spin-coated resists where the lower resist is developed through a chemical process whereas the upper resist is moldable when subjected to a lithographically patterned stamp. An array of openings is made in the top resist by imprinting it with a stamp composed of an array of cylindrical pillars followed by a reactive ion etching (RIE) procedure that ensures that the lower resist is exposed at the bottom of each cylinder. These openings are then extended to the substrate surface using a chemical developer that removes the exposed lower resist while leaving the upper resist unscathed and slightly undercut. In the subsequent Au−Sb deposition, it is this undercut that offers a key advantage in that it creates a disconnect between the material deposited onto the substrate and unwanted material deposited on the sidewalls of the resist. This allows for a crisp and orderly separation of the metal film and resist during the subsequent lift-off process. The newly introduced lithographic procedure, while having added complexity, consistently yields a superior product. Au seeds formed directly on Si_xN_y TEM grid were made by sequentially depositing

continuous layers of Sb (20 nm) and Au (0.2 nm), followed by a heating regimen that sees the temperature raised to 900 °C in 20 min followed by a cooldown to ambient temperatures.

Au NT Synthesis. NT syntheses, which were carried out in a 50 mL Pyrex beaker, proceeded by first adding CTAB (1.5 mL, 10 mM) to Brij 700 (11 mL, 4.1 mM) under the mild stirring brought about by a 1 cm magnetic stir bar rotating at 300 rpm. The Au seed array was then placed at the bottom of the beaker off to one side of the stir bar, after which the solution is heated to 35 °C over a 15 min duration. The synthesis is initiated by injecting aqueous $HAuCl_4$ (1.2 mL, 10 mM) and allowed to proceed for durations that varied depending on the desired NT size. The synthesis is terminated by removing the substrate from the growth solution, rinsing residual chemicals away in DI H_2O and ethanol, and drying it under a N_2 gas flow. The reuse of beakers demanded that they be thoroughly cleaned if the formation of a dense colloid is to be avoided in subsequent syntheses. Used beakers were cleaned in (i) boiling H_2O, (ii) wiped and rinsed with ethanol, acetone, and, H_2O using a lint-free disposable wipe, (iii) exposed to room-temperature aqua regia (Hazard: aqua regia is highly toxic and corrosive) for 3 h, and (iv) thoroughly rinsed in DI water.

Refractive Index Sensitivity. Polarization-dependent refractive index sensitivity measurements were carried out by suspending a NT array in a liquid-filled cuvette. The array was exposed to four different index of refraction mediums composed of acetonitrile, toluene, or combinations thereof with values ranging from 1.346 and 1.496. Refractive index sensitivities were then extracted from the linear slope of LSPR versus refractive index plots. Polarization measurements were taken at 15° intervals.

STEM-EELS Measurements. Low-loss EELS measurements are performed using the Nion aberration-corrected high energy-resolution monochromated EELS-STEM (HERMES) setup located at Oak Ridge National Laboratory. The instrument was operated at an accelerating voltage

of 60 kV with a convergence angle of 30 mrads, a collection angle of 25 mrads, and a beam current of ~10 pA. The scattered electrons are dispersed in a Nion Iris spectrometer at 5 meV per channel with an energy resolution of ~21 meV. EEL spectra and maps were aligned and then normalized with respect to the ZLP in the selected energy window.

Simulations. NT extinction spectra were simulated using the finite-element method (FEM) available through the COMSOL® Multiphysics software package. The geometrical model used for NTs resembles that shown in the inset to Figure 3d where the NT thickness was held constant at X nm, its edge length was varied between 100 and 300 nm, and the (100) side-faceting took on the angles demanded for its intersection with the top and bottom (111) planar surfaces. All NT corners were rounded to prevent unrealistically high near-fields. The optical response was calculated for light having its electric field polarized in various directions parallel to the (111) surface of the NT. Additional details regarding simulations can be found elsewhere.[73]

Instrumentation. Secondary electron SEM images were obtained using a Helios G4 Ux SEM/FIB workstation (FEI). TEM images and the associated SAED patterns were acquired using a Spectra 30-300 (S)TEM (ThermoFisher Scientific) operating at 300 keV. Topographical and stick-slip AFM data utilized a Cypher ES AFM (Oxford instruments) equipped with XXX silicon tips. Spectroscopic data was obtained using a JASCO V−730 UV−visible spectrophotometer fitted with linear polarizers. Au seed preparation utilized a (i) home-built nanoimprinter,[44] (ii) Laurell spin coater, (iii) SAMCO RIE-1C reactive ion etcher, (iv) model 681 Gatan high resolution ion beam coater and (v) Lindberg Blue M furnace fitted with a quartz tube and an Ar gas handling system.

Acknowledgments

This work was supported by the National Science Foundation, Division of Chemistry, Macromolecular, Supramolecular, and Nanochemistry (MSN) Program under Grant No. CHE−2107728 to SN. The AFM investigations (MRS) were supported by …..The computational calculations (JA) were conducted with support of the UCloud services provided by the eScience Center at SDU. The EELS work (VK, JPC) is supported by the Air Force Office of Scientific Research under Award FA9550-21-1-0282. Any opinions, findings, and conclusions or recommendations expressed in this material are those of the authors and do not necessarily reflect the views of the United States Air Force. The STEM-EELS experiments were conducted at the Center for Nanophase Materials Sciences, which is a DOE Office of Science User Facility. This research was conducted, in part, using instrumentation within ORNL's Materials Characterization Core provided by UT-Battelle, LLC, under Contract No. DE-AC05-00OR22725 with the DOE, and sponsored by the Laboratory Directed Research and Development Program of Oak Ridge National Laboratory, managed by UT-Battelle, LLC, for the U.S. Department of Energy. WJT acknowledges support received through a Notre Dame Materials Science and Engineering Fellowship. The work has benefitted from the facilities available through the Notre Dame Integrated Imaging Facility (NDIIF) and the expertise of F. T. Limpoco (Oxford Instruments Asylum Research) in AFM imaging.

Conflict of Interest

The authors declare no conflict of interest.

Data Availability Statement

The data that support the findings of this study are available from the corresponding author upon reasonable request.

References

[1] R. D. Neal, R. A. Hughes, A. S. Preston, S. D. Golze, T. B. Demille, S. Neretina, Substrate-Immobilized Noble Metal Nanoplates: A Review of Their Synthesis, Assembly, and Application. *J. Mater. Chem. C* **2021,** *9*, 12974.

[2] T. Wang, M. Park, Q. Yu, J. Zhang, Y. Yang, Stability and Synthesis of 2D Metals and Alloys: A Review. *Mater. Today Adv.* **2020**, *8*, 100092.

[3] Y. Chen, Z. Fan, Z. Zhang, W. Niu, C. Li, N. Yang, B. Chen, H. Zhang, Two-Dimensional Metal Nanomaterials: Synthesis, Properties, and Applications. *Chem. Rev.* **2018**, *118*, 6409.

[4] X. Hong, C. Tan, J. Chen, Z. Xu, H. Zhang, Synthesis, Properties and Applications of One- and Two-Dimensional Gold Nanostructures. *Nano Res.* **2015**, *8*, 40.

[5] J. E. Millstone, S. J. Hurst, G. S. Métraux, J. I. Cutler, C. A. Mirkin, Colloidal Gold and Silver Triangular Nanoprisms. *Small* **2009**, *5*, 646.

[6] I. Pastoriza-Santos, L. M. Liz-Marzán, Colloidal Silver Nanoplates. State of the Art and Future Challenges. *J. Mater. Chem.* **2008**, *18*, 1724.

[7] X. Cui, F. Qin, Q. Ruan, X. Zhuo, J. Wang, Circular Gold Nanodisks with Synthetically Tunable Diameters and Thicknesses. *Adv. Funct. Mater.* **2018**, *28*, 1705516.

[8] Y. Zhai, J. S. DuChene, Y.-C.Wang, J. Qiu, A. C. Johnston-Peck, B.You, W. Guo, B. DiCiaccio, K. Qian, E. W. Zhao, F. Ooi, D. Hu, D. Su, E. A. Stach, Z. Zhu, W. D. Wei, Polyvinylpyrrolidone-Induced Anisotropic Growth of Gold Nanoprisms in Plasmon-Driven Synthesis. *Nat. Mater.* **2016**, *15*, 889.

[9] T. B. Demille, R. D. Neal, A. S. Preston, Z. Liang, A. G. Oliver, R. A. Hughes, S. Neretina, Epitaxially Aligned Single-Crystal Gold Nanoplates Formed in Large-Area Arrays at High Yield. *Nano Res.* **2022**, *15*, 296.

[10] X. Huang, S. Z. Li, Y. Z. Huang, S. X. Wu, X. Z. Zhou, S. Z. Li, C. L. Gan, F. Boey, C. A. Mirkin, H. Zhang, Synthesis of Hexagonal Close-Packed Gold Nanostructures. *Nat. Commun.* **2011**, *2*, 292.

[11] F. Kiani, G. Tagliabue, High Aspect Ratio Au Microflakes via Gap-Assisted Synthesis. *Chem. Mater.* **2022,** *34*, 1278.

[12] E. Krauss, R. Kullock, X. Wu, P. Geisler, N. Lundt, M. Kamp, B. Hecht, Controlled Growth of High-Aspect-Ratio Single-Crystalline Gold Platelets. *Cryst. Growth Des.* **2018**, *18*, 1297.

[13] F. Muench, R. Popovitz-Biro, T. Bendikov, Y. Feldman, B. Hecker, M. Oezaslan, I. Rubinstein, A. Vaskevich, Nucleation-Controlled Solution Deposition of Silver Nanoplate Architectures for Facile Derivatization and Catalytic Applications. *Adv. Mater.* **2018**, *30*, 1805179.

[14] Y. Yoo, S. I. Kim, S. Han, H. Lee, J. Kim, H. S. Kim, J. P. Ahn, T. Kang, J. Choo, B. Kim, Epitaxially Aligned Submillimeter-Scale Silver Nanoplates Grown by Simple Vapor Transport. *Nanoscale* **2019**, *11*, 17436.

[15] S. D. Golze, S. Porcu, C. Zhu, E. Sutter, P. C. Ricci, E. C. Kinzel, R. A. Hughes, S. Neretina, Sequential Symmetry-Breaking Events as a Synthetic Pathway for Chiral Gold Nanostructures with Spiral Geometries. *Nano Lett.* **2021**, *21*, 2919.

[16] Y. Zhai, F. Zhang, B. Zhang, X. Gao, Engineering Single Nanopores on Gold Nanoplates by Tuning Crystal Screw Dislocation. *Adv. Mater.* **2017**, *29*, 1703102.

[17] W. Guo, A. Johnston-Peck, Y. Zhang, Y. Hu, J. Huang, W. D. Wei, Cooperation of Hot Holes and Surface Adsorbates in Plasmon-Driven Anisotropic Growth of Gold Nanostars. *J. Amer. Chem. Soc.* **2020**, *142*, 10921.

[18] A. Losquin, L. F. Zagonel, V. Myroshnychenko, B. Rodríguez-González, M. Tencé, L. Scarabelli, J. Förstner, L. M. Liz-Marzán, F. J. García de Abajo, O. Stéphan, M. Kociak, Unveiling Nanometer Scale Extinction and Scattering Phenomena through Combined Electron Energy Loss Spectroscopy and Cathodoluminescence Measurements. *Nano Lett.* **2015**, *15*, 1229.

[19] W. Hermoso, T. V. Alves, C. C. S. de Oliveira, E. G. Moriya, F. R. Ornellas, P. H. C. Camargo, Triangular Metal Nanoprisms of Ag, Au, and Cu: Modeling the Influence of Size, Composition, and Excitation Wavelength on the Optical Properties. *Chem. Phys.* **2013**, *423*, 142.

[20] F. Qin, T. Zhao, R. Jiang, N. Jiang, Q. Ruan, J. Wang, L. D. Sun, C.-H. Yan, H.-Q. Lin, Thickness Control Produces Gold Nanoplates with Their Plasmon in the Visible and Near-Infrared Regions. *Adv. Optical Mater.* **2016**, *4*, 76.

[21] Y. Huang, A. R. Ferhan, Y. Gao, A. Dandapat, D. H. Kim, High-Yield Synthesis of Triangular Gold Nanoplates with Improved Shape Uniformity, Tunable Edge Length and Thickness. *Nanoscale* **2014**, *6*, 6496.

[22] E. Hao, G. C. Schatz, Electromagnetic Fields around Silver Nanoparticles and Dimers. *J. Chem. Phys.* **2004**, *120*, 357.

[23] Y. Y. Tanaka, T. Shimura, Tridirectional Polarization Routing of Light by a Single Triangular Plasmonic Nanoparticle. *Nano Lett.* **2017**, *17*, 3165.

[24] M. M. Islam, M. M. Hossen, T. Koschny, A. C. Hillier, Shape- and Orientation-Dependent Scattering of Isolated Gold Nanostructures Using Polarized Dark-Field Microscopy. *J. Phys. Chem. C* **2021**, *125*, 11478.

[25] Z. Li, Y. Yu, Z. Chen, T. Liu, Z. K. Zhou, J. B. Han, J. Li, C. Jin, X. Wang, Ultrafast Third-Order Optical Nonlinearity in Au Triangular Nanoprism with Strong Dipole and Quadrupole Plasmon Resonance. *J. Phys. Chem. C* **2013**, *117*, 20127.

[26] X. Cui, Y. Lai, F. Qin, L. Shao, J. Wang, H. Q. Linc, Strengthening Fano Resonance on Gold Nanoplates with Gold Nanospheres. *Nanoscale* **2020**, *12*, 1975.

[27] T. Tan, S. Zhang, J. Wang, Y. Zheng, H. Lai, J. Liu, F. Qin, C. Wang, Resolving the Stacking Fault Structure of Silver Nanoplates. *Nanoscale* **2021**, *13*, 195.

[28] S. Ye, S. D. Connell, J. R. McLaughlan, L. Roach, Z. Aslam, N. Chankhunthod, A. P. Brown, R. Brydson, R. J. Bushby, K. Critchley, P. L. Coletta, A. F. Markham, S. D. Evans, One-Step Preparation of Biocompatible Gold Nanoplates with Controlled Thickness and Adjustable Optical Properties for Plasmon-Based Applications. *Adv. Funct. Mater*. **2020**, *30*, 2003512.

[29] G. K. Joshi, P. J. McClory, S. Dolai, R. Sardar, Improved Localized Surface Plasmon Resonance Biosensing Sensitivity Based on Chemically-Synthesized Gold Nanoprisms as Plasmonic Transducers. *J. Mater. Chem.* **2012**, *22*, 923.

[30] L. Scarabelli, L. M. Liz-Marzán, An Extended Protocol for the Synthesis of Monodisperse Gold Nanotriangles. *ACS Nano* **2021**, *15*, 18600.

[31] C. Zhao, G. Wang, T. Takarada, X. Liang, M. Komiyama, M. Maeda, Shape-Selective Isolation of Au Nanoplates from Complex Colloidal Media by Depletion Flocculation. *Colloids and Surf. A* **2019**, *568*, 216.

[32] Z. Sun, A. Umar, J. Zeng, X. Luo, L. Song, Z. Zhang, Z. Chen, J. Li, F. Su, Y. Huang, Highly Pure Gold Nanotriangles with almost 100% Yield for Surface-Enhanced Raman Scattering. *ACS Appl. Nano Mater.* **2022**, *5*, 1220.

[33] H. Zhang, C. Kinnear, P. Mulvaney, Fabrication of Single-Nanocrystal Arrays. *Adv. Mater.* **2020**, *32*, 1904551.

[34] R. A. Hughes, E. Menumerov, S. Neretina, When Lithography Meets Self-Assembly: A Review of Recent Advances in the Directed Assembly of Complex Metal Nanostructures on Planar and Textured Surfaces. *Nanotechnology* **2017**, *28*, 282002.

[35] S. V. Grayli, X. Zhang, F. C. MacNab, S. Kamal, D. Star, G. W. Leach, Scalable, Green Fabrication of Single-Crystal Noble Metal Films and Nanostructures for Low-Loss Nanotechnology Applications. *ACS Nano* **2020**, *14*, 7581.

[36] H. Zhang, Y. Liu, M. F. S. Shahidan, C. Kinnear, F. Maasoumi, J. Cadusch, E. M. Akinoglu, T. D. James, A. Widmer-Cooper, A. Roberts, P. Mulvaney, Direct Assembly of Vertically Oriented, Gold Nanorod Arrays. *Adv. Funct. Mater.* **2021**, *31*, 2006753.

[37] F. Liebig, R. M. Sarhan, M. Sander, W. Koopman, R. Schuetz, M. Bargheer, J. Koetz, Deposition of Gold Nanotriangles in Large Scale Close-Packed Monolayers for X-ray-Based Temperature Calibration and SERS Monitoring of Plasmon-Driven Catalytic Reactions. *ACS Appl. Mater. Interfaces* **2017**, *9*, 20247.

[38] L. Scarabelli, M. Coronado-Puchau, J. J. Giner-Casares, J. Langer, L. M. Liz-Marzán, Monodisperse Gold Nanotriangles: Size Control, Large-Scale Self-Assembly, and Performance in Surface-Enhanced Raman Scattering. *ACS Nano* **2014**, *8*, 5833.

[39] Y. H. Lee, C. K. Lee, B. Tan, J. M. Rui Tan, I. Y. Phang, X. Y. Ling, Using the Langmuir–Schaefer Technique to Fabricate Large-Area Dense SERS-Active Au Nanoprism Monolayer Films. *Nanoscale* **2013**, *5*, 6404.

[40] Q.-Y. Lin, J. A. Mason, Z. Li, W. Zhou, M. N. O'Brien, K. A. Brown, M. R. Jones, S. Butun, B. Lee, V. P. Dravid, K. Aydin, C. A. Mirkin, Building Superlattices from Individual Nanoparticles via Template-Confined DNA-Mediated Assembly. *Science* **2018**, *359*, 669−672.

[41] Y. Zhou, X. Zhou, D. J. Park, K. Torabi, K. A. Brown, M. R. Jones, C. Zhang, G. C. Schatz, C. A. Mirkin, Shape-Selective Deposition and Assembly of Anisotropic Nanoparticles. *Nano Lett.* **2014**, *14*, 2157.

[42] S. R. Beeram, F. P. Zamborini, Purification of Gold Nanoplates Grown Directly on Surfaces for Enhanced Localized Surface Plasmon Resonance Biosensing. *ACS Nano* **2010**, *4*, 3633−3646.

[43] S. D. Golze, R. A. Hughes, S. Rouvimov, R. D. Neal, T. B. Demille, S. Neretina, Plasmon-Mediated Synthesis of Periodic Arrays of Gold Nanoplates using Substrate-Immobilized Seeds Lined with Planar Defects. *Nano Lett.* **2019**, *19*, 5653.

[44] E. Menumerov, S. D. Golze, R. A. Hughes, S. Neretina, Arrays of Highly Complex Noble Metal Nanostructures using Nanoimprint Lithography in Combination with Liquid-Phase Epitaxy. *Nanoscale* **2018**, *10*, 18186.

[45] P. Farzinpour, A. Sundar, K. D. Gilroy, Z. E. Eskin, R. A. Hughes, S. Neretina, Dynamic Templating: A Large Area Processing Route for the Assembly of Periodic Arrays of Sub–Micrometer and Nanoscale Structures. *Nanoscale* **2013**, *5*, 1929.

[46] S. D. Golze, R. A. Hughes, E. Menumerov, S. Rouvimov, S. Neretina, Synergistic Roles of Vapor- and Liquid-Phase Epitaxy in the Seed-Mediated Synthesis of Substrate-Based Noble Metal Nanostructures. *Nanoscale* **2021**, *13*, 20225.

[47] K. D. Gilroy, A. Sundar, M. Hajfathalian, A. Yaghoubzade, T. Tan, D. Sil, E. Borguet, R. A. Hughes, S. Neretina, Transformation of Truncated Gold Octahedrons into Triangular Nanoprisms through the Heterogeneous Nucleation of Silver. *Nanoscale* **2015**, *7*, 6827.

[48] S. Griffin, N. P. Montoni, G. Li, P. J. Straney, J. E. Millstone, D. J. Masiello, J. P. Camden, Imaging Energy Transfer in Pt-Decorated Au Nanoprisms via Electron Energy-Loss Spectroscopy. *J. Phys. Chem. Lett.* **2016,** *7*, 3825.

[49] U. Hohenester, Simulating Electron Energy Loss Spectroscopy with the MNPBEM Toolbox. *Comput. Phys. Commun.* **2014,** *185*, 1177.

[50] A. Campos, A. Arbouet, J. Martin, D. Gérard, J. Proust, J. Plain, M. Kociak, Plasmonic Breathing and Edge Modes in Aluminum Nanotriangles. *ACS Photonics* **2017,** *4*, 1257.

[51] V. Kumar, J. P. Camden, Imaging Vibrational Excitations in the Electron Microscope. *J. Phys. Chem. C* **2022,** *Accepted*. DOI Needed

[52] V. Myroshnychenko, J. Rodríguez-Fernández, I. Pastoriza-Santos, A. M. Funston, C. Novo, P. Mulvaney, L. M. Liz-Marzán, F. J. García de Abajo, Modelling the Optical Response of Gold Nanoparticles. *Chem. Soc. Rev.* **2008,** *37*, 1792.

[53] Y. Yoo, H. Lee, H. Lee, M. Lee, S. Yang, A. Hwang, S.-i. Kim, J. Y. Park, J. Choo, T. Kang, B. Kim, Surfactant-Free Vapor-Phase Synthesis of Single-Crystalline Gold Nanoplates for Optimally Bioactive Surfaces. *Chem. Mater.* **2017**, *29*, 8747.

[54] R. Long, S. Zhou, B. J. Wiley, Y. Xiong, Oxidative Etching for Controlled Synthesis of Metal Nanocrystals: Atomic Addition and Subtraction. *Chem. Soc. Rev.,* **2014**, *43*, 6288.

[55] C. L. Haynes, A. D. McFarland, L. Zhao, R. P. Van Duyne, G. C. Schatz, L. Gunnarsson, J. Prikulis, B.Kasemo, M. Käll, Nanoparticle Optics: The Importance of Radiative Dipole Coupling in Two-Dimensional Nanoparticle Arrays. *J. Phys. Chem. B* **2003**, *107*, 7337.

[56] R. Jin, Y. C. Cao, E. Hao, G. S. Métraux, G. C. Schatz, C. A. Mirkin, Controlling Anisotropic Nanoparticle Growth through Plasmon Excitation. *Nature* **2003**, *425*, 487.

[57] Y. He, G. Shi, Surface Plasmon Resonances of Silver Triangle Nanoplates: Graphic Assignments of Resonance Modes and Linear Fittings of Resonance Peaks. *J. Phys. Chem. B* **2005,** *109,* 17503.

[58] K. L. Kelly, E. Coronado, L. L. Zhao, G. C. Schatz, The Optical Properties of Metal Nanoparticles: The Influence of Size, Shape, and Dielectric Environment. *J. Phys. Chem. B* **2003**, *107*, 668.

[59] J. Lee, J. W. Ha, Elucidating the Contribution of Dipole Resonance Mode to Polarization Dependent Optical Properties in Single Triangular Gold Nanoplates. *Chem. Phys. Lett.* **2018**, *713*, 121.

[60] K. L. Shuford, M. A. Ratner, G. C. Schatz, Multipolar Excitation in Triangular Nanoprisms. J. *Chem. Phys.* **2005**, *123*, 114713.

[61] K. W. Smith, J. Yang, T. Hernandez, D. F. Swearer, L. Scarabelli, H. Zhang, H. Zhao, N. A. Moringo, W. S. Chang, L. M. Liz-Marzán, E. Ringe, P. Nordlander, S. Link, Environmental Symmetry Breaking Promotes Plasmon Mode Splitting in Gold Nanotriangles. *J. Phys. Chem. C* **2018**, *122*, 13259.

[62] C. Awada, T. Popescu, L. Douillard, F. Charra, A. Perron, H. Yockell-Lelièvre, A.-L. Baudrion, P. M. Adam, R. Bachelot, Selective Excitation of Plasmon Resonances of Single Au Triangles by Polarization-Dependent Light Excitation. *J. Phys. Chem. C* **2012**, *116*, 14591.

[63] L. Lu, S. Zou, B. Fang, The Critical Impacts of Ligands on Heterogeneous Nanocatalysis: A Review. *ACS Catal.* **2021**, *11*, 6020.

[64] N. A. Hatab, C. M. Rouleau, S. T. Retterer, G. Eres, P. B. Hatzingerd, B. Gu, An Integrated Portable Raman Sensor with Nanofabricated Gold Bowtie Array Substrates for Energetics Detection. *Analyst* **2011**, *136*, 1697.

[65] H. Duan, H. Hu, K. Kumar, Z. Shen, J. K. W. Yang, Direct and Reliable Patterning of Plasmonic Nanostructures with Sub-10-nm Gaps. *ACS Nano* **2011**, *5*, 7593.

[66] A. J. Haes, S. Zou, G. C. Schatz, R. P. Van Duyne, Nanoscale Optical Biosensor: Short Range Distance Dependence of the Localized Surface Plasmon Resonance of Noble Metal Nanoparticles. *J. Phys. Chem. B* **2004**, *108*, 6961.

[67] B. J. Y. Tan, C. H. Sow, T. S. Koh, K. C. Chin, A. T. S. Wee, C. K. Ong, Fabrication of Size-Tunable Gold Nanoparticles Array with Nanosphere Lithography, Reactive Ion Etching, and Thermal Annealing. *J. Phys. Chem. B* **2005**, *109*, 11100.

[68] J.-S. Huang, V. Callegari, P. Geisler, C. Brüning, J. Kern, J. C. Prangsma, X. Wu, T. Feichtner, J. Ziegler, P. Weinmann, M. Kamp, A. Forchel, P. Biagioni, U. Sennhauser, B. Hecht, Atomically Flat Single-Crystalline Gold Nanostructures for Plasmonic Nanocircuits. *Nat. Comm.* **2010**, *1*, 150.

[69] B. Hoffmann, M. Y. Bashouti, T. Feichtner, M. Mačković, C. Dieker, A. M. Salaheldin, P. Richter, O. D. Gordan, D. R. T. Zahn, E. Spiecker, S. Christiansen, New Insights into Colloidal Gold Flakes: Structural Investigation, Micro-Ellipsometry and Thinning Procedure towards Ultrathin Monocrystalline Layers. *Nanoscale* **2016**, *8*, 4529.

[70] L. Shao, Y. Tao, Q. Ruan, J. Wang, H. Q. Lin, Comparison of the Plasmonic Performances between Lithographically Fabricated and Chemically Grown Gold Nanorods. *Phys. Chem. Chem. Phys.* **2015**, *17*, 10861.

[71] T. Siegfried, Y. Ekinci, O. J. F. Martin, H. Sigg, Engineering Metal Adhesion Layers That Do Not Deteriorate Plasmon Resonances. *ACS Nano* **2013**, *7*, 2751

[72] R. D. Nagel, S. Filser, T. Zhang, A. Manzi, K. Schönleber, J. Lindsly, J. Zimmermann, T. L. Maier, G. Scarpa, K. Krischer, P. Lugli, Nanoimprint Methods for the Fabrication of Macroscopic Plasmonically Active Metal Nanostructures. *J. Appl. Phys.* **2017**, *121*, 084305.

[73] Z. L. Lawson, A. S. Preston, M. T. Korsa, N. L. Dominique, W. J. Tuff, E. Sutter, J. P. Camden, J. Adam, R. A. Hughes, S. Neretina, Plasmonic Gold Trimers and Dimers with Air-Filled Nanogaps. *ACS Appl. Mater. Interfaces* **2022**, *14*, 28186.

TOC Graphic and Text

Table of Contents Entry. The deterministic positioning of single-crystal plasmonic nanostructures into organized configurations represents a foundational capability for the advancement of wafer-based technologies. In this work, a benchtop nanofabrication route is presented for the formation of large-area arrays of gold nanotriangles. The route is unique in that it avoids colloid-to-substrate transfers, instead opting for the direct synthesis of nanotriangles on substrate surfaces.

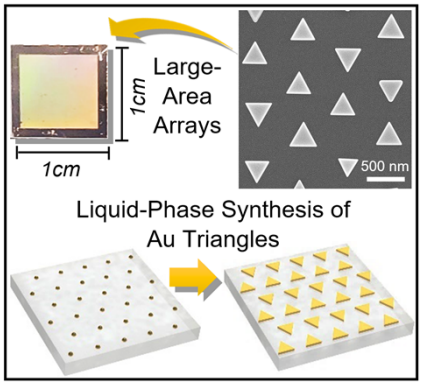

Supporting Information

Large-Area Periodic Arrays of Atomically Flat Single-Crystal Gold Nanotriangles formed Directly on Substrate Surfaces

Robert D. Neal,[†] Zachary R. Lawson,[†] Walker J. Tuff,[†] Kaikui Xu,[†] Vishal Kumar,[‡] Matiyas T. Korsa,[§] Maksym Zhukovskyi,[∥] Matthew R. Rosenberger,[†] Jost Adam,[§] Jon P. Camden,[‡] Robert A. Hughes,[†] and Svetlana Neretina[†‡]*

[†] College of Engineering, University of Notre Dame, Notre Dame, Indiana 46556, United States

[‡] Department of Chemistry and Biochemistry, University of Notre Dame, Notre Dame, Indiana 46556, United States

[§] Computational Materials Group, SDU Centre for Photonics Engineering, Mads Clausen Institute, University of Southern Denmark, 5230 Odense, Denmark

[∥] Notre Dame Integrated Imaging Facility, University of Notre Dame, Notre Dame, Indiana 46556, USA

*E-mail: sneretina@nd.edu

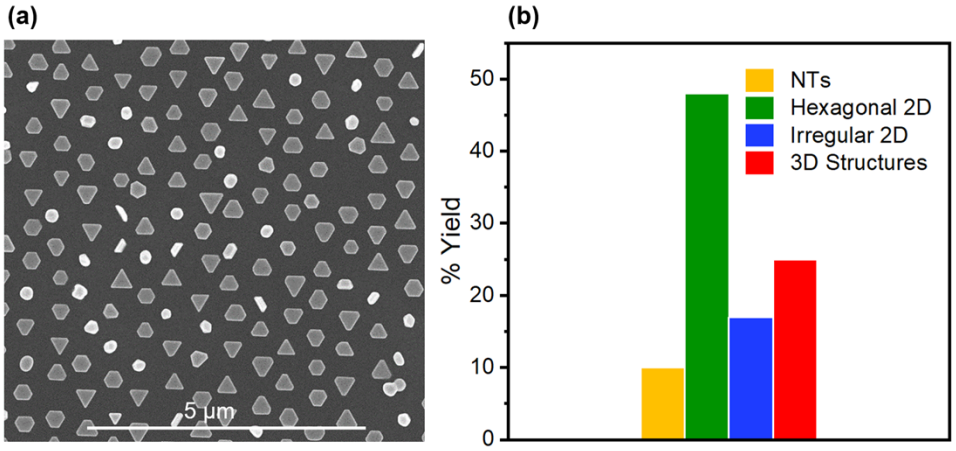

Figure S1. SEM image of an array of structures formed when the NT synthesis is carried out in the absence of CTAB. It should be noted that hexagon nanoplate growth is favored under these conditions.

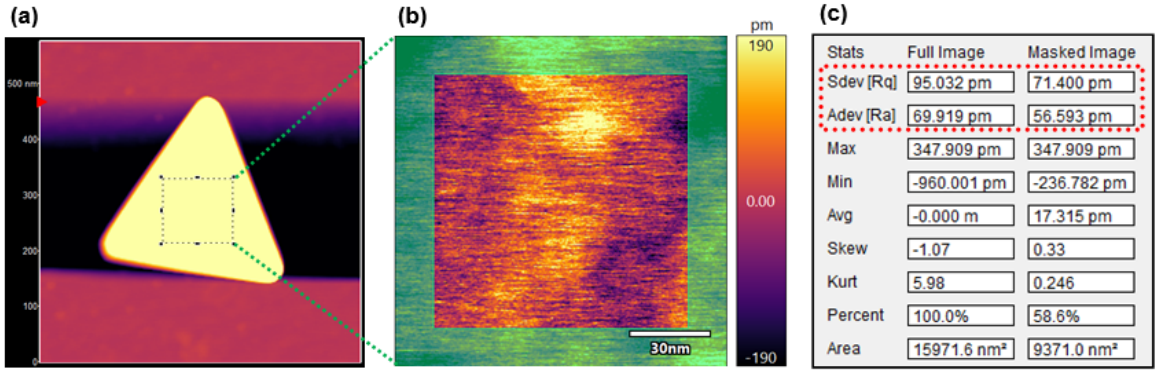

Figure S2. AFM images of (a) an entire Au NT and (b) the masked central region on its top surface. (c) Experimental parameters showing that the top surface is exceptionally smooth with root-mean-square (Rq) and average roughnesses (Ra) of 71.40 and 56.59 pm, respectively.

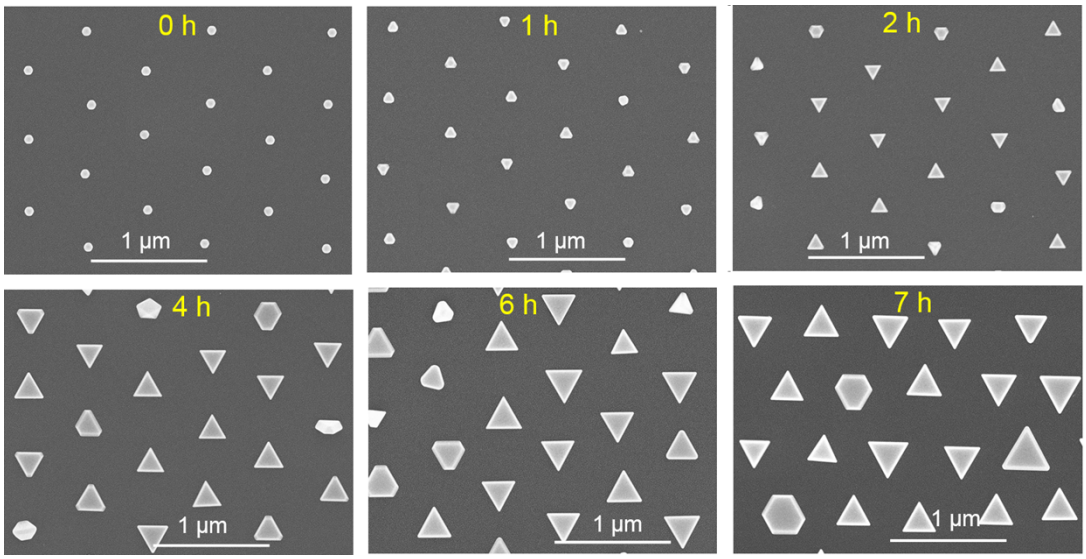

Figures S3. SEM images showing the time progression in NT size for synthesis times ranging from 1 to 7 h. The 0 h image shows a seed array that has never been exposed to the NT growth solution.

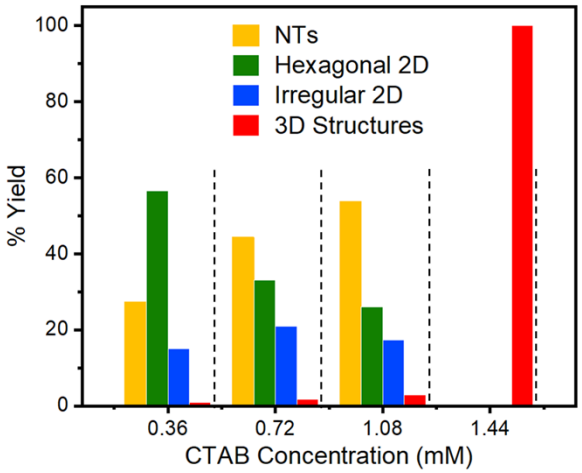

Figure S4. Histogram showing the shape distribution of arrayed structures as a function of CTAB concentration. Observed is an increase in NT yields up to 1.08 mM that is accompanied by a decline in the yield of hexagonal nanoplates. At the 1.44 CTAB concentration, growth is inhibited to the extent that the structures retain the three-dimensional character of the seed. It should be noted that the software used to assess nanostructure shape is quite stringent in that NTs with one truncated corner can result in its designation as an irregular 2D structure.

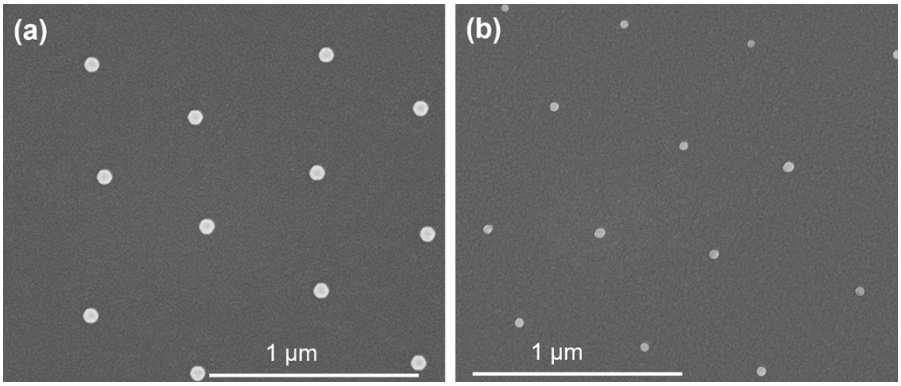

Figure S5. SEM images comparing (a) Au seeds and (b) identical Au seeds that have been exposed for 6 h to a NT "growth solution" in which high concentrations of CTAB (2.55 mM) were used. It should be noted that this high CTAB concentrations results in a reduction in seed size.

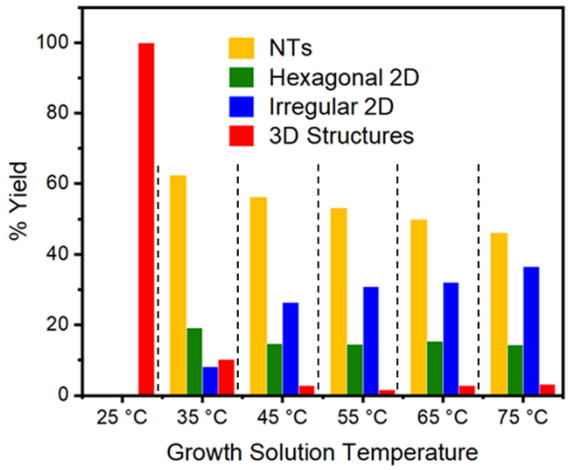

Figure S6. Histogram showing the shape distribution of the arrayed structures as a function of the growth temperature. It reveals that the yield of NTs is maximum for syntheses carried out at 35 °C. As temperature is increased, the NT yield steadily decreases as the number of irregularly shaped nanoplates increases. This finding likely indicates that CTAB gradually loses its ability to preserve the correct NT side faceting as the temperature and the associated lateral growth rate are increased. At 25 °C, growth is inhibited to the extent that all of the seeds retain their three-dimensional character.

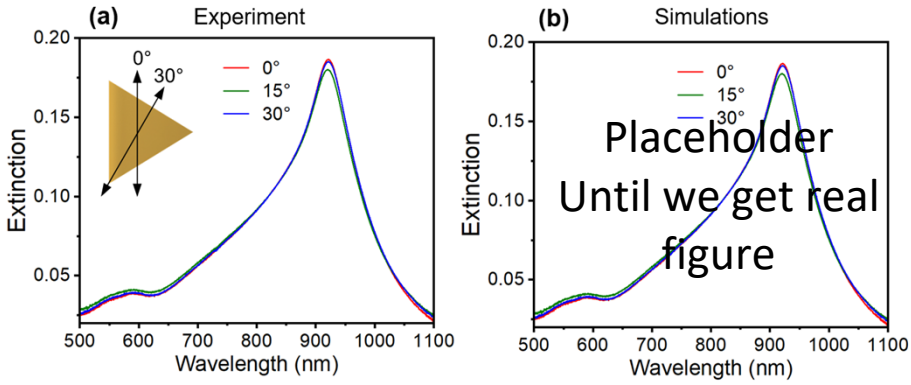

Figure S7. (a) Experimental and (b) simulated extinction spectra showing that the LSPR position is independent of the polarization angle.

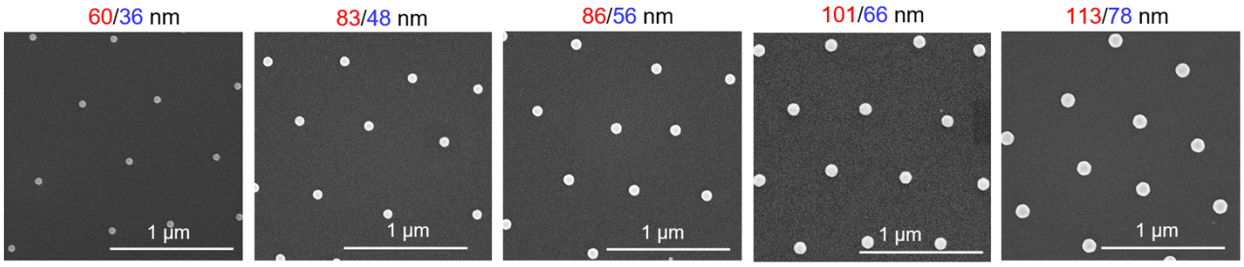

Figure S8. SEM images of Au seed arrays showing that the nanostructure size can be systematically varied. The average seed diameter (red) and height (blue) as derived from AFM and SEM images is provided for each of the arrays.

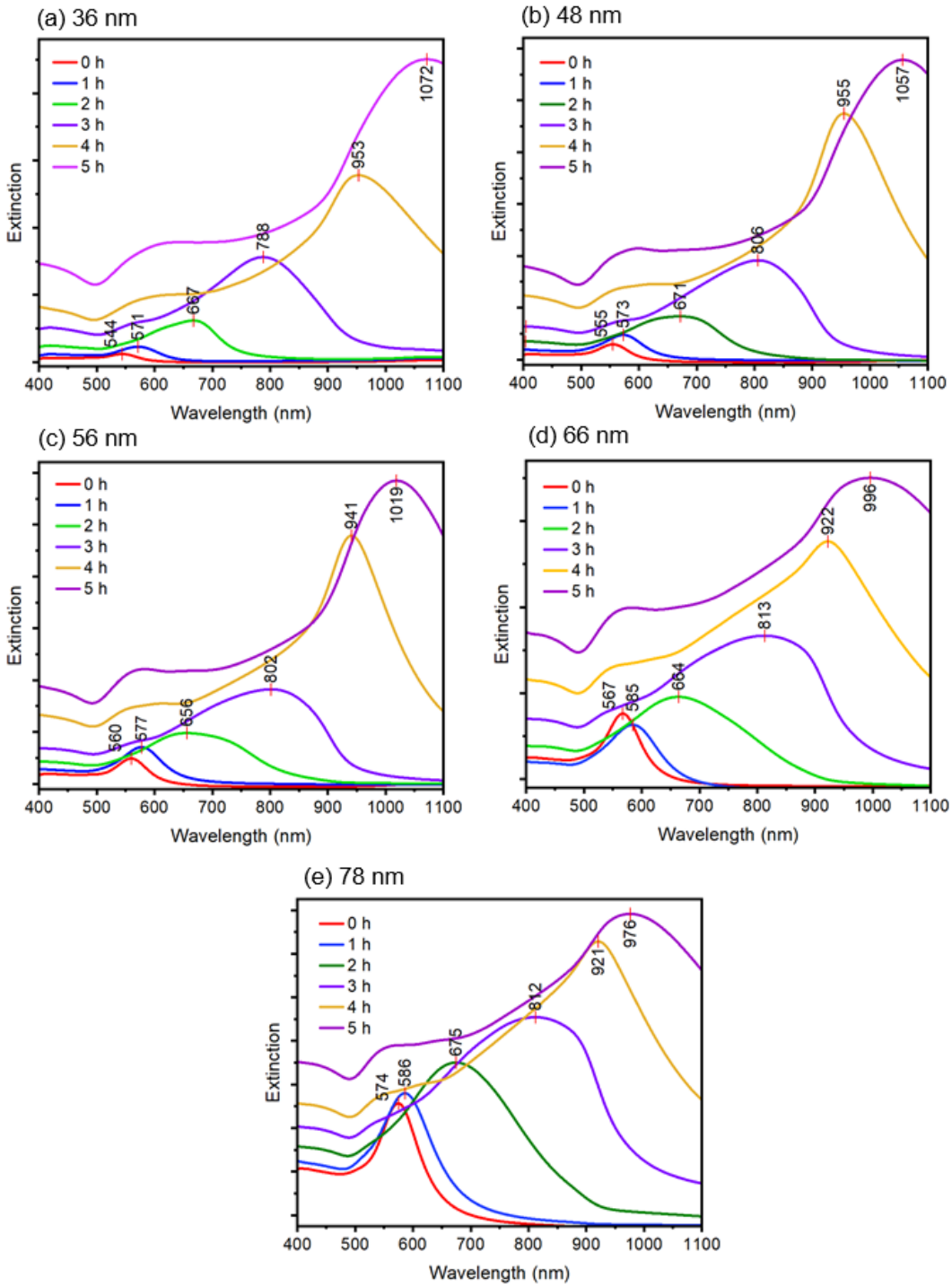

Figure S9. Time-dependent extinction spectra for NT growths lasting 6 h that are derived from seeds with heights of (a) 36, (b) 48, (c) 56, (d) 66, and (e) 78 nm.